J Therm Spray Tech
https://doi.org/10.1007/s11666-026-02159-9

ORIGINAL RESEARCH ARTICLE

High-Resolution Synchrotron μXRD and μXRF for Local Phase and Elemental Analysis in Suspension Plasma Sprayed Environmental Barrier Coatings

Chinmayee Nayak[1] · Arman Hasani[1] · Gidla Vinay[1] · Ermei Mäkilä[1] · Ebenezer Owusu[4] · Nikhil Kamboj[1] · Malgorzata Grazyna Makowska[3] · Alex Lynam[4] · Acacio Rincon Romero[4] · Sneha Goel[2] · Tanvir Hussain[4] · Antti Salminen[1] · Ashish Ganvir[1]

Submitted: 5 July 2025 / in revised form: 19 December 2025 / Accepted: 5 January 2026

Abstract Suspension plasma spraying (SPS) enables the fabrication of environmental barrier coatings (EBCs) with complex multilayer architectures; however, degradation in such systems often initiates locally at buried interfaces, making it difficult to resolve using conventional laboratory-scale characterization techniques. In this work, the applicability of synchrotron-based micro-x-ray diffraction (μXRD), combined with micro-x-ray fluorescence (μXRF), is evaluated for the characterization of SPS-deposited ytterbium disilicate (YbDS) EBCs. An as-sprayed YbDS coating was investigated as a baseline case to examine differences between conventional XRD and spatially resolved μXRD, while an annealed and CMAS-exposed YbDS coating was studied as a service-relevant case to probe localized phase evolution. The samples were selected from previously optimized SPS process conditions and are not intended for direct comparison. Laboratory-scale XRD provided global phase information, whereas μXRD enabled layer-specific phase identification and resolved localized interfacial features. In the as-sprayed condition, μXRD confirmed phase-pure YbDS, resolved the crystallinity of individual coating layers, and verified the absence of unintended interfacial reaction phases that are not accessible by conventional XRD. In the annealed + CMAS-exposed coating, μXRD and μXRF revealed the formation of a calcium–ytterbium–silicate oxyapatite phase confined to the YbDS/Si interface, highlighting the localized nature of CMAS-induced degradation. These results demonstrate that synchrotron microanalysis provides valuable

This article is an invited paper selected from presentations at the 2025 International Thermal Spray Conference, held May 5–8, 2025, in Vancouver, Canada, and has been expanded from the original presentation. The issue was organized by Giovanni Bolelli, University of Modena and Reggio Emilia (Lead Editor); Fardad Azarmi, North Dakota State University; Sara Bagherifard, Politecnico di Milano; Partha Pratim Bandyopadhyay, Indian Institute of Technology, Kharagpur; Šárka Houdková, University of West Bohemia; Heli Koivuluoto, Tampere University; Yuk-Chiu Lau, General Electric Power (Retired); Hua Li, Ningbo Institute of Materials Technology and Engineering, CAS; Sinan Müftü, Northeastern University; and Filofteia-Laura Toma, Fraunhofer Institute for Material and Beam Technology.

✉ Chinmayee Nayak
chinmayee.nayak@utu.fi

Ashish Ganvir
gmashish19@gmail.com; ashish.ganvir@utu.fi

[1] Research Group of Digital Manufacturing and Surface Engineering, Department of Mechanical and Materials Engineering, University of Turku, FI-20500 Turku, Finland

[2] Advanced Materials for Nuclear Energy, VTT Technical Research Centre of Finland, Espoo, Finland

[3] Laboratory for Synchrotron Radiation and Femtochemistry and Laboratory for Nuclear Materials, Advanced Nuclear Materials Group, Paul Scherrer Institute, 5232 Villigen PSI, Switzerland

[4] Centre of Excellence in Coatings & Surface Engineering, Faculty of Engineering, University of Nottingham, University Park, Nottingham NG7 2RD, UK

Published online: 08 February 2026

complementary insight for probing localized phase evolution in thermally sprayed EBC systems.

Keywords environmental barrier coating · micro-XRD and micro-XRF · suspension Plasma spraying

Introduction

Gas turbine engines play a pivotal role in modern industry, powering both aerospace propulsion systems and energy generation units. Traditionally, these engines have relied heavily on nickel-based superalloys, known for their strength and reliability under high temperatures. However, the operational ceiling of these materials is inherently constrained by their melting point (~1350 °C), limiting their service temperature to around 1100 °C (Ref 1). As industrial demands for improved thermal efficiency and fuel economy intensify, particularly under cyclic thermal loading, the need for next-generation materials has become increasingly evident.

Ceramic matrix composites (CMCs), especially those based on silicon carbide (SiC), have emerged as highly attractive alternatives due to their exceptional thermal stability, superior strength-to-weight ratio, excellent hardness, and outstanding oxidation resistance in dry oxygen environments (Ref 2, 3). Despite these advantages, SiC-based CMCs suffer rapid degradation in the presence of steam and corrosive deposits such as calcium–magnesium–alumino–silicates (CMAS), commonly encountered in combustion environments (Ref 4). The degradation mechanism is primarily a recession process, wherein SiC oxidizes to form a protective SiO_2 scale. This scale, however, reacts with high-temperature steam to produce volatile $Si(OH)_4$ gas, leading to surface material loss at rates approaching 1 µm/hour (Ref 5). Additionally, molten CMAS originating from ambient dust or fuel impurities reacts aggressively with both the protective SiO_2 layer and the SiC matrix, compounding the material's vulnerability (Ref 6).

To counteract these effects, the development of robust environmental barrier coatings (EBCs) has become essential. Effective EBCs must satisfy a stringent set of requirements: (1) thermal expansion compatibility with the substrate, (2) chemical stability and inertness, (3) high-temperature phase stability, (4) controlled silica volatilization, and (5) resistance to CMAS infiltration (Ref 7). Among the candidate materials, ytterbium disilicate (YbDS) has attracted considerable attention due to its excellent CTE match with SiC, good chemical stability, and reasonable resistance to silica volatilization and CMAS interaction (Ref 8). Nevertheless, YbDS is not immune to CMAS-induced degradation. Upon exposure, it chemically reacts with CMAS to form calcium–ytterbium–silicate (Ca-Yb-Si) apatite phases, which lead to coating recession, crack initiation, and interfacial porosity (Ref 9, 10). These microstructural defects significantly undermine the integrity and durability of the EBC system, emphasizing the need to closely examine localized phase evolution and reaction zones at the coating–CMAS interface.

While traditional characterization techniques such as laboratory-scale x-ray diffraction (XRD) are frequently employed to study EBCs (Fig. 1a), they are often inadequate for analyzing subsurface and interfacial phenomena. Conventional XRD is limited by its shallow penetration depth (~30 µm), large beam spot size (~8 mm^2), and fixed sample geometry, making it ill-suited for detecting localized or fine-scale phase transformations (Ref 11. In contrast, synchrotron-based techniques, particularly micro-XRD (Fig. 1b) offer significantly improved spatial resolution and analytical depth. With a focused beam size of approximately 1 μm^2 and higher photon energy (~18.2 keV at 0.68 Å wavelength), micro-XRD enables detailed structural analysis of both surface and buried interfaces. Furthermore, sample rotation during scanning allows for comprehensive orientation mapping, providing rich insights into localized phase development within the coating architecture (Ref 12, 13).

The primary objective of the present work is to understand the applicability and added value of synchrotron-based micro-x-ray diffraction (µXRD) and micro-x-ray fluorescence (µXRF) for the characterization of suspension plasma sprayed (SPS) ytterbium disilicate environmental barrier coatings. In particular, this work aims to assess what additional structural and chemical information µXRD can provide beyond conventional laboratory-scale XRD when applied to heterogeneous, multilayer EBC architectures. Therefore, two YbDS-based coating systems were selected strategically from previously optimized and published SPS process conditions (Ref 14). An as-sprayed YbDS coating was examined as a baseline case to directly assess differences between conventional laboratory-scale XRD and localized synchrotron µXRD analysis within the same coating architecture. In addition, an annealed and CMAS-exposed YbDS coating was investigated as a second, independent case study representing realistic service-relevant conditions, since EBCs in practical applications are typically crystallized prior to exposure and operate in CMAS-containing environments (Ref 15).

These two samples are therefore not intended to be directly compared to each other in a process–property sense. Instead, they serve complementary purposes in demonstrating the capability of synchrotron µXRD and µXRF to resolve localized phase evolution, buried interfacial reactions, and early-stage degradation features in

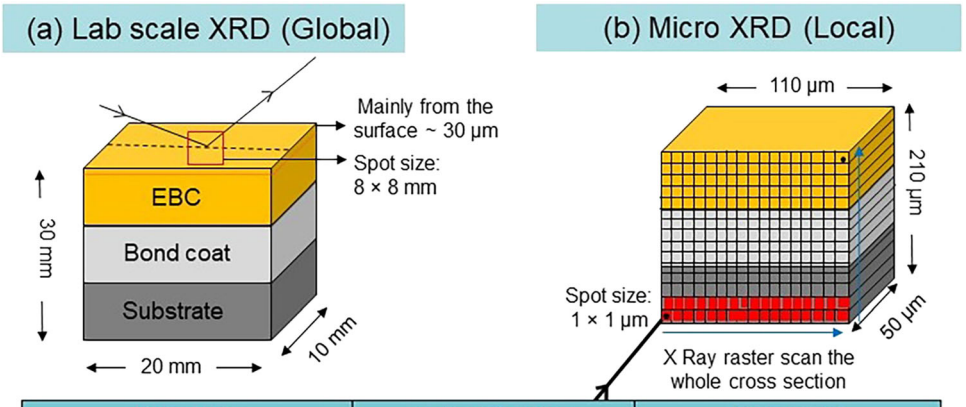

Fig. 1 Schematic comparison between (a) Laboratory-scale XRD and (b) synchrotron micro-XRD (This penetration depth is for the used material, otherwise it is strongly material dependent)

Parameters	Lab scale XRD	Micro XRD
Wavelength	λ = 1.5406 Å (Cu Kα1)	λ = 0.6812 Å (Synchroton)
Energy	8.05 KeV	18.2 KeV
Spot Size	8 × 8 mm	1 × 1 µm
X- Ray penetration depth	~ 30 µm	~ 50 to 60 µm

SPS EBC systems that remain inaccessible to conventional laboratory characterization techniques.

Materials and Methods

Preparation of Coatings

The feedstock materials used in this study consisted of high-purity commercial silicon

(Si) powder (99.9 %, 15-75 µm; Metco, USA) for the bond coat deposition and a commercial suspension of ytterbium disilicate (YbDS) containing 40 wt.% solids in water (Treibacher AG, Austria) (Ref 14). The dried powder derived from the suspension exhibited predominantly angular morphology with characteristic particle sizes below 5 µm. Stainless steel (bought from store of University of Nottingham, 60 × 25 × 3mm^3) and reaction-bonded silicon carbide (RbSiC) disks (Jai Engineers, UK), with dimensions of 12.7 mm in diameter and 2.8 mm in thickness, and used as the substrate material for (1) as-sprayed YbDS coating and (2) annealed + CMAS-exposed YbDS coating, respectively. Steel substrate was used for as-sprayed YbDS coating for process optimization. Prior to coating, the stainless-steel and RbSiC substrates were grit-blasted using 60 µm silicon carbide particles at a pressure of 9 bar to promote adhesion. The resulting surface roughness of the substrates was measured by Alicona profilometry (5G Infinite Focus, Bruker, Germany) and obtained to be Ra = 5.0 ± 0.1 µm, and Ra = 3.1 ± 0.1 µm, respectively.

A bilayer coating system was deposited on both steel and RbSiC substrates, consisting of an initial silicon (Si) bond coat followed by a YbDS top coat. The silicon bond coat was deposited on steel and RbSiC substrate using atmospheric plasma spraying (APS) SG-100 plasma spray gun connected with powder feeder (Praxair Surface Technology, USA). The coating was deposited using a spray power of 27 kW, a current of 600 A, 85 psi pressure of Argon (Ar) as primary gas, 35 psi pressure of hydrogen (H_2) as secondary gas, and a stand-off-distance of 120 mm. The detailed parameters are reported in the previous study (Ref 14).

The YbDS top coat was deposited onto the silicon bond-coated steel and RbSiC substrates using suspension plasma spraying (SPS) with a three-cathode, high-power Axial-III torch (Northwest Mettech Corp., Canada). The plasma was operated with argon (Ar) as the primary gas and nitrogen (N_2) as the secondary gas. The ratio of Ar:N_2 was kept 80:20 and 70:30 for steel and RbSiC substrates, respectively. The stand-off distance and number of passes used were 100 mm and 40, respectively. The net power was varied by varying the Ar:N_2 gas ratio (70:30 and 80:20), thereby modifying the plasma enthalpy, which governs net power and influences different coating thickness and thermal stresses in the coating. Detailed information regarding the YbDS coating process and related parameters is available in a previous publication (Ref 14).

Post-Treatment and CMAS Exposure

The as-sprayed YbDS (with Si bond coat and RbSiC substrate) sample first annealed via subjecting to a

crystallization heat-treatment in box furnace (Elite Thermal Systems Ltd, UK) at 1200 °C for 2 h with heating and cooling rates of 5 °C/min (Ref 14). Subsequently, the annealed YbDS sample was exposed to CMAS (35 CaO-10 MgO-7 Al_2O_3-48 SiO_2 in mol %). The annealed YbDS sample with CMAS were placed on 22 mm sapphire disks (PI-KEM, UK) and heat-treated at 1300 °C in air (CMAS melting point ~1250 °C) in the box furnace using heating and cooling rates of 10 °C/min for 5 mins. The samples were allowed to cool in the furnace to room temperature as described elsewhere (Ref 14). The short CMAS exposure duration (5 minutes) employed in this study to investigate the early-stage infiltration behavior of molten CMAS into the EBC system, rather than the long-term phase stability of corrosion products (Ref 16). In CMAS–EBC interactions, infiltration kinetics represent the initial and governing stage of degradation, which subsequently leads to chemical reactions and secondary phase formation during prolonged exposure (Ref 17–19). Longer-term CMAS exposures aimed at studying reaction product evolution and coating recession will be addressed in future work.

Cross-sections of both samples were prepared using the following procedure. The as-sprayed YbDS (with steel substrate) and annealed + CMAS-exposed YbDS (with RbSiC substrate) specimens were first cold mounted under vacuum impregnation using EpoFix resin and hardener (Struers, Denmark). The mounted samples were then cut into two halves using high precision cutting machine (QATM, Germany) and abrasive diamond cut-off wheels (Metprep, UK) with a cutting speed of 0.025 mm/s. One of the resulting pieces of the sectioned samples was subsequently cold mounted again. The cut faces of the samples were ground using a 200-grit diamond lapping disk (DK Holdings Ltd, UK) and polished using polishing pads and diamond paste of 6 µm and then 1 µm to achieve the desired surface finish.

Material Characterization

Laboratory-scale x-Ray Diffraction (XRD)

Laboratory-scale XRD was performed on powder and as-sprayed YbDS and annealed + CMAS-exposed YbDS samples for the phase identification using a D8 Advance Da Vinci diffractometer (Bruker, Germany) with Cu cathode (wavelength of 1.5406 Å) using Bragg–Brentano scanning mode. The angular range investigated was from 10° to 70° with a step size set to 0.02° and a dwell time of 0.3 s for all the measurements.

Scanning Electron Microscope (SEM)

SEM analysis of the surface topography and cross-sectional microstructure of the as-sprayed and annealed + CMAS-exposed coatings was performed using a Quanta 600 SEM (FEI Europe, Netherlands) and a JSM-7100F FEG-SEM (JEOL Ltd., UK). Elemental composition was analyzed with an AZtec EDS system equipped with an X-Max 150 detector (Oxford Instruments, UK). Coating porosity was quantified using the open-source FIJI (ImageJ) software (Ref 20) from ten backscattered electron (BSE) images acquired at 1000 × magnification from representative cross-sectional regions, and is reported as the mean with the corresponding standard error. FIB-prepared micro-samples were further examined by FE-SEM (APREO, Thermo Fisher Scientific, USA) coupled with EDS.

Synchrotron Micro-x-ray Diffraction (µXRD)/ Micro-x-ray Fluorescence (µXRF)

Sample preparation for synchrotron µXRD/µXRF: A focused ion beam (FIB) was used to prepare a sample from the as-sprayed YbDS and annealed + CMAS-exposed YbDS samples for micro-characterization. This process involved a xenon (Xe +) ion beam at 30 kV for milling and 12 kV for carbon deposition, which attached the manipulator to the micro-sample for lift-out and mounting on a pin for x-ray measurements. As illustrated in Fig. 2, the sample preparation involved several steps, yielding final dimensions (height × width × thickness) of 80 µm × 73.04 µm × 50 µm for the as-sprayed YbDS coating and 110 µm × 210 µm × 50 µm for the annealed + CMAS-exposed coating. The 50 µm thickness was selected based on the x-ray beam energy and the absorption characteristics of the materials, while the chosen height ensures that all coating layers along with a portion of the substrate are included. However, the substrate in the as-sprayed YbDS sample (Fig. 2e) is not shown, as the substrate itself being stainless steel is not relevant for EBC. For this sample, the focus is on examining local phase changes in the YbDS top coat, the Si bond coat, and their interface.

Overview SEM micrographs of the FIBed cross-section of as-sprayed YbDS coating and the annealed + CMAS-exposed YbDS coating are presented in Fig. 3a and b, respectively. In Fig. 3a, the magenta- and blue-dotted rectangles highlight the YbDS top coat (50 µm) and the silicon bond coat (23.04 µm), respectively, while the interface between these two layers is indicated by a white-dotted rectangle. Figure 3d further identifies structural regions, with the magenta-, green-, and blue-dotted rectangles corresponding to the YbDS top coat (120 µm), silicon bond coat (80 µm), and the RbSiC substrate (10 µm),

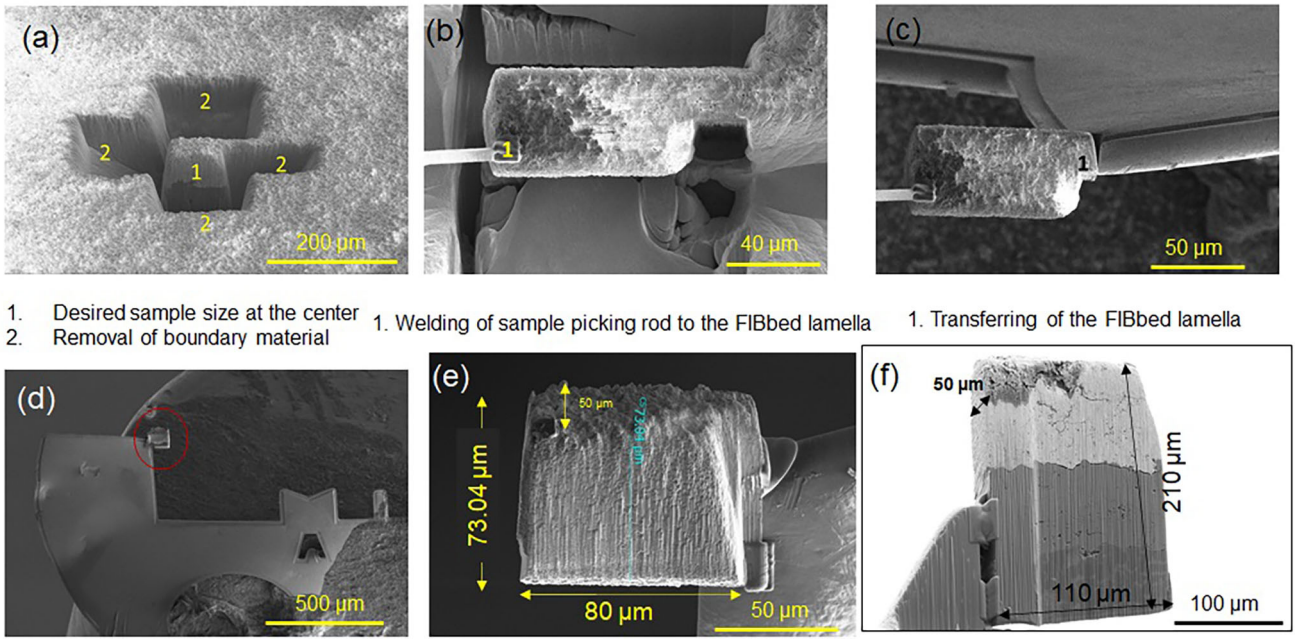

Fig. 2 FIB milling process steps: (a) Locating a region and placing milling patterns, top–down milled micro-sample, (b) Bridge holding the micro-sample in place (c) Removing the bridge, (d) FIB milling to create a suitable mounting site at the tip of the pin, (e) Final FIB-milled as-sprayed YbDS coating micro-sample ready for the synchrotron micro-characterization, (f) Final FIB-milled annealed + CMAS-exposed YbDS coating micro-sample ready for the synchrotron micro-characterization

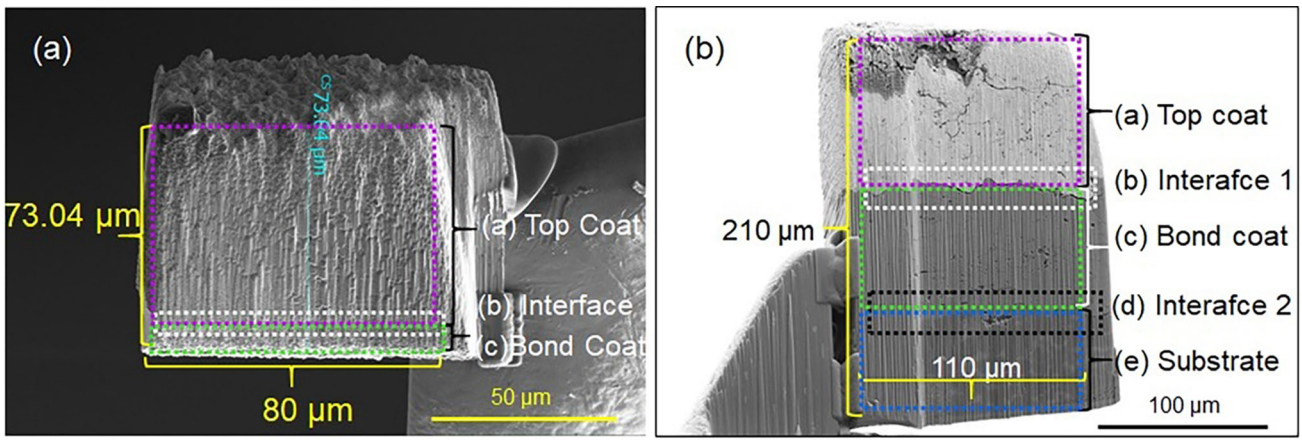

Fig. 3 Scanning electron microscope (SEM) of overview of FIBed cross-sections micro-samples of (a) as-sprayed YbDS coating, and (b) annealed + CMAS-exposed YbDS coating ready for the synchrotron micro-characterization

respectively. In Fig. 3b, the white- and black-dotted rectangles mark interface 1 (between the YbDS top coat and the Si bond coat) and interface 2 (between the Si bond coat and the RbSiC-based substrate). In the as-sprayed YbDS coating (Fig. 3a), the steel substrate is not visible in the FIB-prepared sample, as the current work does not focus on the stainless-steel substrate or its interface. The primary aim of using the as-sprayed YbDS coating (with steel substrate) in the present work was to identify local phase changes using synchrotron analysis within the YbDS top coat, the silicon bond coat, and their interface in as-sprayed condition. In contrast, the annealed + CMAS-exposed sample (Fig. 3b) includes the intended substrate (i.e., RbSiC) for the EBC coating, and 10 µm of the RbSiC substrate are visible in the FIB-prepared section. Synchrotron-based µXRD and µXRF contrast microscopy were performed at the micro-XAS beamline of the Swiss Light Source (PSI) to understand localized phase and elemental analysis across the coating layers and their interfaces. A detailed methodology and measurement setup of the synchrotron-based µXRD and µXRF facility is shown (Ref 21)in our previous publication (Ref 21).

XRD data were collected using a Dectris Eiger 4 M single-photon counting detector, while XRF measurements were acquired via four silicon drift detectors (SDDs) positioned around the sample. During raster scanning across the ceramic cross-sections, simultaneous μXRD and μXRF measurements were carried out, with the experimental setup illustrated by Arman et al. (Ref 21). The incident x-ray beam was focused to a 1 μm spot size, and the sample was scanned in 0.5 μm steps along the x and y directions normal to the beam using a sample manipulator, with a 200 ms acquisition time per step. The x-ray beam wavelength was set to 0.6812 Å. Scanning covered the entire area of the FIB-prepared samples, generating 1 × 1 μm pixel resolution images. Azimuthal integration of the resulting diffraction rings was performed using the pyFAI Python library (Ref 22), and each integrated pattern was mapped to a corresponding pixel, yielding approximately 3000 XRD images with intensities at specific diffraction angles. Simultaneously, XRF spectra were recorded from each pixel and analyzed using the PyMca software package (Ref 23), enabling spatial mapping of elemental distributions. Together, the μXRD and μXRF datasets provide complementary insights into the sample's crystalline structure and elemental composition. Further evaluation of diffraction patterns from selected regions was conducted using ImageJ (Fiji) software (version 1.53q). Crystalline phases were identified through Rietveld refinement using X'Pert HighScore Plus (version 4.9) and Topas 6 (Bruker).

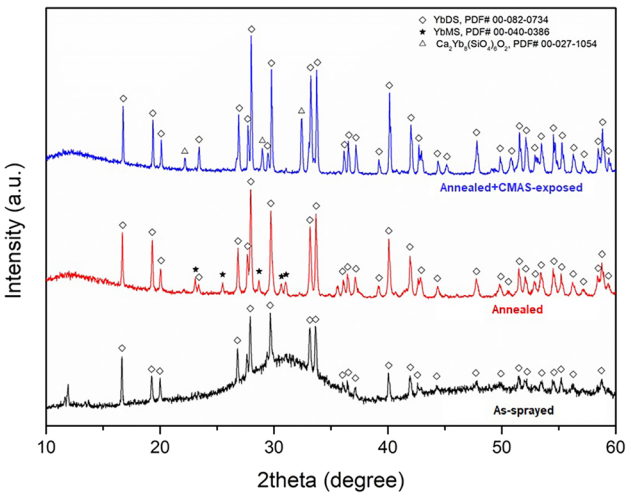

Fig. 4 XRD pattern of YbDS coating in as-sprayed, annealed, and annealed + CMAS-exposed conditions

Results

Basic Characterization and Phase Analysis

The laboratory-scale XRD was performed on the YbDS top coatings of both the samples (x-ray penetration depth is nearly 30 μm). The XRD plots (Fig. 4) disclosed the phase compositions of YbDS top coat in as-sprayed (black curve), annealed (red curve) and annealed + CMAS-exposed (blue curve) conditions. The as-sprayed coatings also display solely YbDS peaks. In addition to the crystalline signals, it exhibits two distinct broad humps in their XRD patterns, centered around 30° and 55°, indicative of an amorphous component (Ref 24. Upon annealing, this amorphous phase undergoes crystallization, resulting in coatings that are predominantly crystalline. As shown in Fig. 4, both the annealed (red curve) and annealed + CMAS-exposed (blue curve) samples display prominent YbDS peaks along with minor reflections attributable to ytterbium monosilicate (YbMS), (Ref 25, 26) matching ICDD PDF #00-040-0386. The Rietveld analysis revealed the composition of the annealed YbDS top coat as a material mixture of 82.5 wt.% ytterbium disilicate (YbDS) and 17.5 wt.% ytterbium monosilicate (YbMS) (Ref 14). The formation of YbMS is due to extreme thermal environment during plasma spraying partially decomposes or volatilizes the disilicate, shifting the local chemistry toward the monosilicate phase (Ref 27). The YbDS and YbMS contents in the as-sprayed coatings could not be quantified, as the presence of amorphous phases rendered the Rietveld phase analysis unreliable. However, following exposure to CMAS for 5 minutes, the diffraction peaks of YbMS disappear. Instead, the XRD pattern of the annealed + CMAS-exposed coating reveals the formation of a new phase. This newly identified phase is attributed to a reaction between CMAS and YbDS, and is consistent with the formation of a hexagonal silicate oxyapatite compound, $Ca_2Yb_8(SiO_4)_6O_2$ (Ref 28), matching ICDD PDF #00-027-1050.

The cross-sectional BSE SEM micrographs of the as-sprayed YbDS and the annealed + CMAS-exposed YbDS, can be seen in Fig. 5a and b, respectively. The top YbDS coating thickness of as-sprayed YbDS and annealed + CMAS-exposed YbDS samples is different, i.e., 50 μm and 120 μm, respectively, because of different process parameters (Ref 14). The high-magnification SEM micrographs of YbDS coating in as-sprayed and annealed + CMAS-exposed samples are shown in Fig. 5c and d, respectively. The dark gray regions correspond to the YbDS phase, the light gray regions represent the YbMS phase, and the black areas indicate porosity within the coating. The combined effects of annealing and CMAS interaction have notably

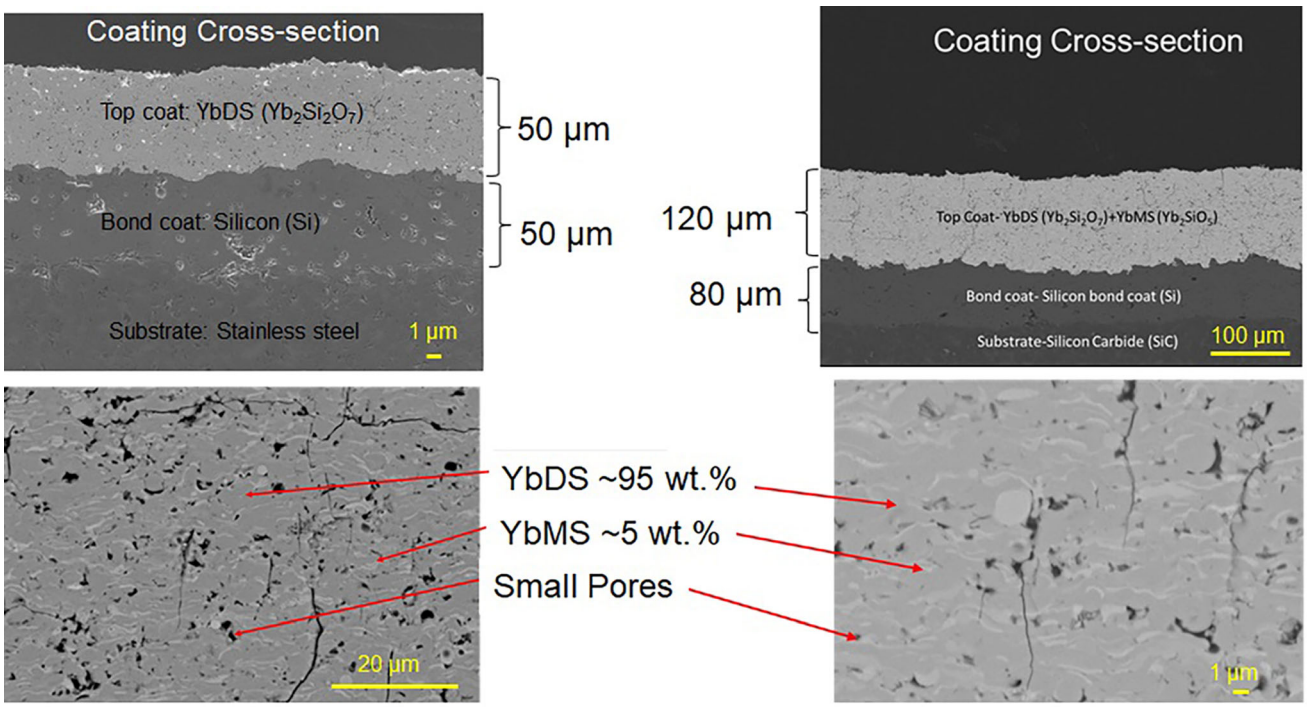

Fig. 5 Cross-sectional views of the coatings: (a) as-sprayed YbDS, (b) annealed + CMAS-exposed YbDS, along with high-magnification microstructures of (c) the as-sprayed YbDS and (d) the annealed + CMAS-exposed YbDS

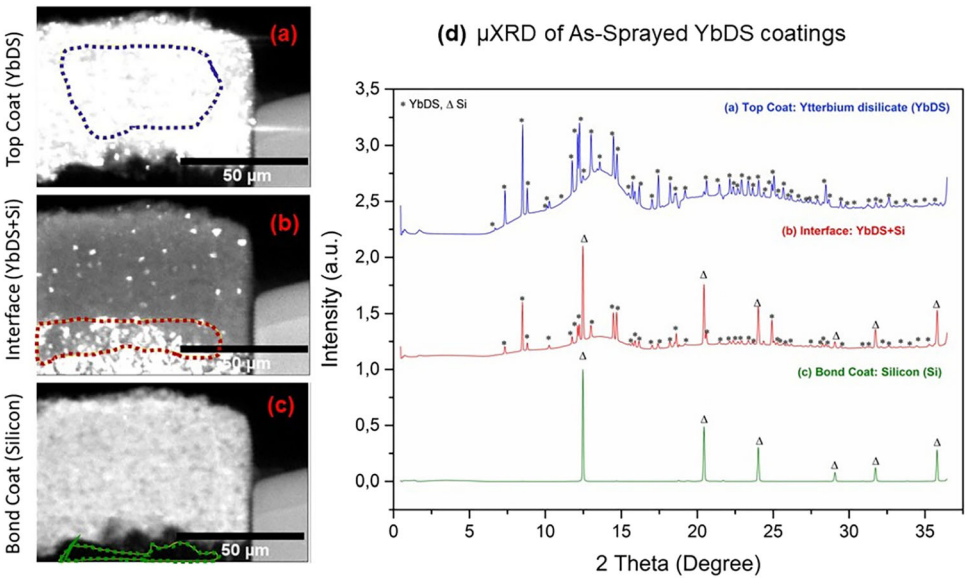

Fig. 6 SEM micrographs of as-sprayed YbDS FIBed micro-sample; (a) YbDS Top-coat, (b) interface between YbDS top coat and Si bond coat, (c) Si bond coat and (d) the associated µXRD diffractograms of each layer

reduced porosity within the coating as evidenced by the micrograph in Fig. 5d. The porosity was measured by using "imageJ" FIJI, and obtained as 14 ± 3% and 5 ± 1% for as-sprayed YbDS (Ar: N_2 = 70:30) and annealed + CMAS-exposed YbDS (Ar:N_2 = 80:20) samples, respectively. (Ref 14). The observed densification contributes to enhanced structural cohesion and is expected to improve both thermal stability and resistance to environmental degradation, critical for performance in high-temperature operating environments.

Synchrotron µXRD, µXRF and Laboratory-Scale EDS

As-Sprayed YbDS Coating

The overview of coatings layers (a) the YbDS top coat, (b) the interface between YbDS and the Si bond coat, and (c) the Si bond coat in FIBed micro-size as-sprayed YbDS sample are displayed in Fig. 6a, b and c, respectively. The µXRD patterns collected from three distinct regions of the as-sprayed EBC system (a) the YbDS top coat (traced in blue) (b) the interface between YbDS and the Si bond coat (traced in red), and (c) the Si bond coat (traced in green). The µXRD analysis of each traced region is shown in Fig. 6d. The µXRD analysis revealed well-defined diffraction peaks corresponding to ytterbium disilicate (YbDS, marked by *) and crystalline silicon (Si, marked by Δ). No additional or undesired phases were detected, confirming phase purity in the as-sprayed state. Notably, the diffraction profiles also showed two broad humps centered approximately at 2θ angle of 12–17° and 18–22°, indicative of a partially amorphous structure. This is characteristic of rapid solidification during the plasma spray process. The diffraction signal from the top coat shows a high degree of phase stability for YbDS, while the interface region displays overlapping signals from both YbDS and the underlying silicon bond coat. In contrast, the bond coat region predominantly shows sharp Si peaks, confirming its crystallinity. The µXRD data confirm that the as-sprayed coatings maintain the intended phase composition and structural integrity, which is critical for thermal and environmental performance in high-temperature applications.

These findings are further validated by the elemental analysis presented in Fig. 7. The SEM image in Fig. 7a reveals the layered microstructure of the coatings, while Fig. 7b shows elemental maps highlighting three distinct regions, marked as areas 1, 2, and 3 for quantitative analysis. The µXRF elemental distribution in Fig. 7c shows a clear spatial gradient, with strong signal intensity localized in the top coat and diminishing toward the bond coat and substrate. The energy dispersive X-ray spectroscopy (EDS) area mapping confirms a distinct distribution of ytterbium concentrated in the top coat (Fig. 7d) and silicon predominantly in the bond coat (Fig. 7e), with no signs of chemical inhomogeneity or phase segregation. The uniform distribution of oxygen (O) and carbon (C) appear uniformly distributed with minor surface-level variation (Fig. 7f and g). The absence of sharp compositional discontinuities or segregated regions indicates a homogeneous as-sprayed microstructure with no evidence of unintended secondary phases.

Quantitative EDS results in Fig. 7h supports these observations. Area 1 (top coat) and area 2 (near the

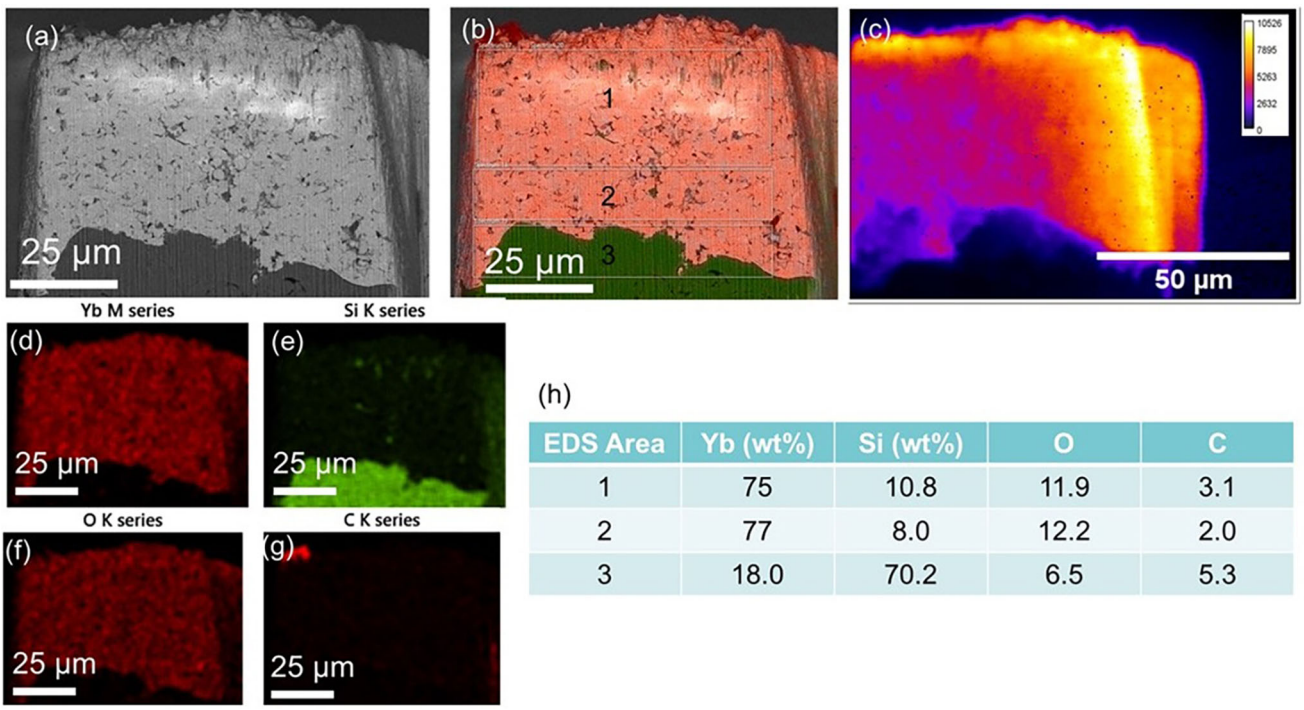

(h)

EDS Area	Yb (wt%)	Si (wt%)	O	C
1	75	10.8	11.9	3.1
2	77	8.0	12.2	2.0
3	18.0	70.2	6.5	5.3

Fig. 7 (a) SEM image of the FIBed as-sprayed YbDS micro-sample; (b) EDS area mapping of the same region; (c) µXRF map showing elemental distribution of Yb ; (d–g) EDS elemental maps highlighting the presence of Yb, Si, O, and C, respectively; (h) Quantitative analysis of elemental composition based on EDS data

interface) exhibit high ytterbium content (75–77 wt.%) with moderate Si content (8–10.8 wt.%), consistent with the expected YbDS composition. In contrast, area 3 (bond coat) displays a reversed profile with dominant Si content (70.2 wt.%) and reduced ytterbium (18 wt.%), verifying the integrity of the bond coat layer. The data clearly show that the coating has the right layering, and they also confirm that the as-sprayed coating is made of clean, stable phases.

Annealed + CMAS-Exposed YbDS Coating

The overview of coatings layers (a) YbDS top coat, the (b) interface between the top coat and the silicon bond coat (interface 1), (c) the silicon bond coat, (d) the interface

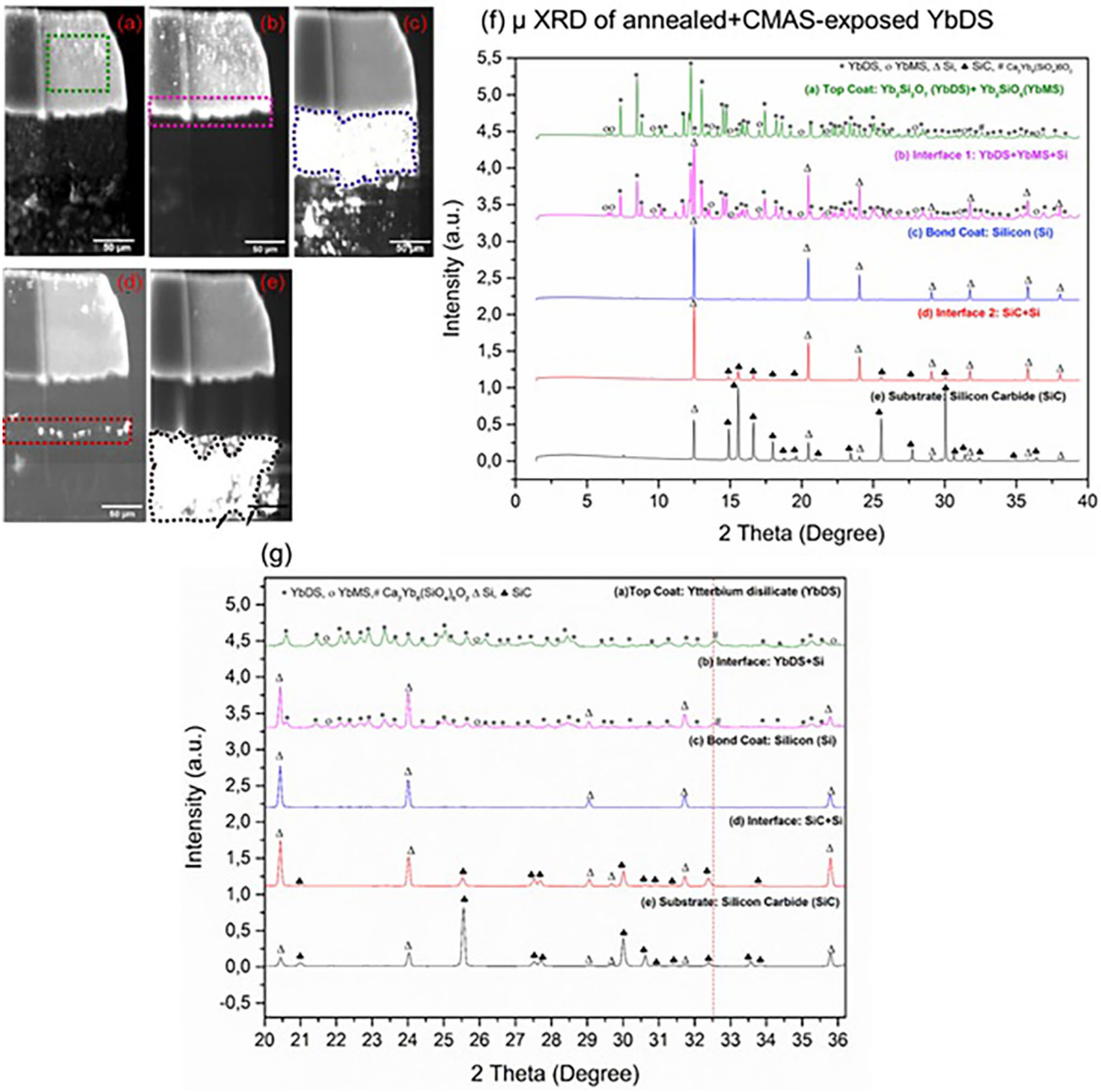

Fig. 8 SEM micrographs of annealed + CMAS-exposed YbDS FIBed micro-sample (a) YbDS top coat layer; (b) interface 1 between the YbDS top coat and the silicon bond coat; (c) Silicon bond coat region; (d) interface 2 between the silicon bond coat and the RbSiC ceramic matrix composite substrate; (e) RbSiC substrate (f) Corresponding micro-XRD diffractograms for each of these layers, (g) Enlarged micro-XRD diffractograms for each of layer, with 2θ between 20° to 36°

between the silicon bond coat and the RbSiC substrate (interface 2), and the (e) RbSiC substrate in FIBed micro-size annealed + CMAS-exposed YbDS sample are displayed in Fig 8a, b, c, d, and e, respectively. The μXRD patterns collected from each distinct regions of the annealed + CMAS-exposed YbDS sample (a) the YbDS top coat (traced in green), (b)interface between the top coat and the silicon bond coat (interface 1) (traced in magenta), (c) the silicon bond coat (traced in purple), (d) the interface between the silicon bond coat and the RbSiC substrate (interface 2) (traced in red), and the (e) RbSiC substrate (traced in black). The correspondence μXRD analysis of traced region is shown in Fig. 8f.

The diffraction pattern of the top coat (Fig. 8f, green curve) reveals a dominant presence of YbDS ($Yb_2Si_2O_7$) along with a minor fraction of YbMS, (Yb_2SiO_5), indicating partial phase transformation during annealing. Notably, additional peaks corresponding to a calcium–ytterbium–silicate oxyapatite phase, $Ca_2Yb_8(SiO_4)_6O_2$, were detected in interface 1 (Fig. 8f, magenta curve), confirming a chemical reaction between infiltrated CMAS and the YbDS matrix. The as-sprayed coating predominantly exhibited amorphous characteristics with clear YbDS peaks (Fig. 6d). In contrast, the annealed + CMAS-exposed sample showed enhanced crystallinity and the presence of a calcium (Ca) rich apatite phase, which is distinctly visible in the micron-scale specimen at a 2θ position of 32.5° (Fig. 8g). These results provide strong evidence of CMAS-induced degradation pathways and the influence of annealing on microstructural stability and phase development within the YbDS-based EBC system.

This phase is characteristic of CMAS corrosion, forming at the interface where CMAS infiltration initiates chemical modification. The silicon bond coat and substrate regions (Fig. 8f, blue curve and black curve) maintain their phase identities, showing sharp reflections of crystalline silicon and silicon carbide, respectively.

The elemental distribution maps and quantitative EDS analysis presented in Fig. 9 provide the evidence of chemical interaction between the YbDS top coat and infiltrated CMAS following annealing. The localized accumulation of calcium is observed at the top coat/bond coat interface (area 2), with Ca content reaching ~ 21.9 wt.%, confirming the formation of a Ca-rich secondary phase. This finding supports the earlier XRD results (Fig. 8g), where the presence of $Ca_2Yb_8(SiO_4)_6O_2$ apatite was identified at 2θ of 32.5° (Ref 29, 30). This Ca-rich region represents the nucleation zone for CMAS-induced degradation, as the chemical infiltration modifies the stoichiometry of the coating, triggering secondary phase formation. The distinct boundary between Yb-rich and Ca-rich zones, along with the sharp Ca peak in μXRF (Fig. 8g), highlights that the degradation is localized yet structurally disruptive, particularly at the interface where thermal and chemical stresses are highest.

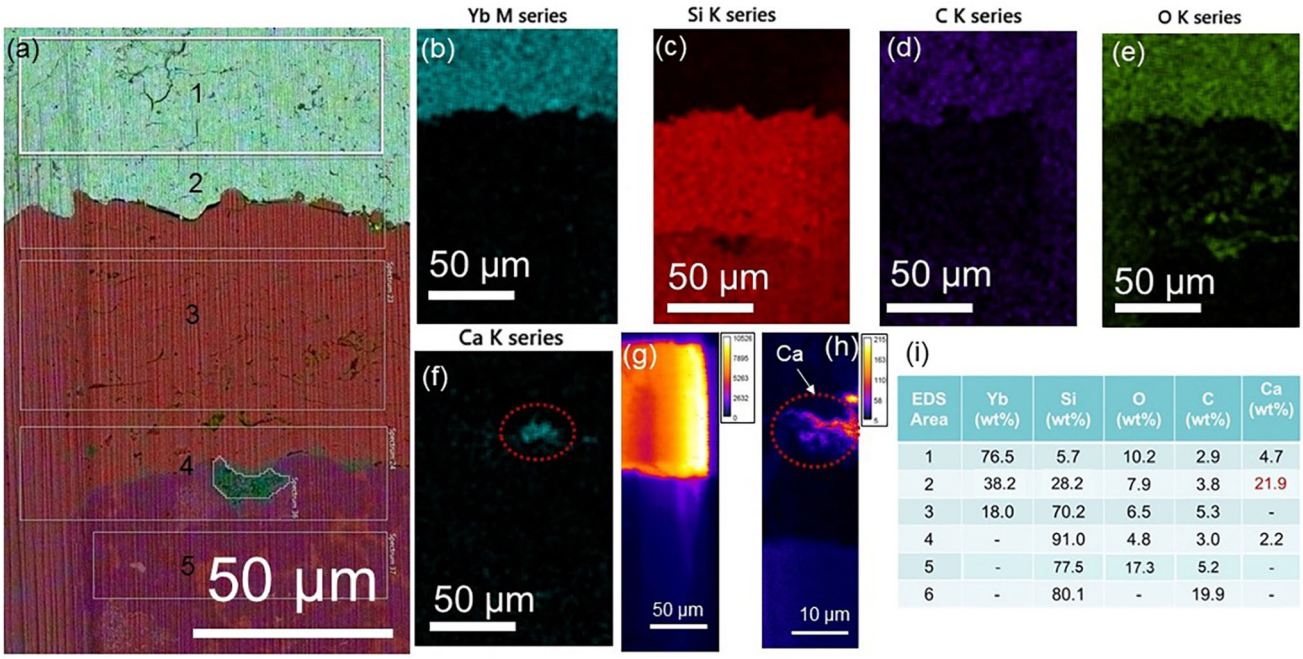

EDS Area	Yb (wt%)	Si (wt%)	O (wt%)	C (wt%)	Ca (wt%)
1	76.5	5.7	10.2	2.9	4.7
2	38.2	28.2	7.9	3.8	21.9
3	18.0	70.2	6.5	5.3	-
4	-	91.0	4.8	3.0	2.2
5	-	77.5	17.3	5.2	-
6	-	80.1	-	19.9	-

Fig. 9 (a) EDS area mapping of the annealed + CMAS-exposed FIBed micro-sample; (b-f) EDS elemental maps highlighting the presence of Yb, Si, C, O, and Ca, respectively; (g-h) μXRF map showing elemental distribution of Yb and Ca (dark orange); (i) Quantitative analysis of elemental composition based on EDS data

These observations suggest that while the bulk of the top and bond coats remain chemically stable, the interface is the most vulnerable zone, where CMAS corrosion initiates coating failure. The presence of the apatite phase here compromises the bond strength and long-term durability of the EBC. Overall, these results reinforce the critical importance of interface engineering and the need for CMAS-resistant top coat materials or barrier layers to suppress reactive infiltration under service conditions.

Discussions

EBC deposited by SPS exhibit complex multilayer architectures and microstructural heterogeneity, in which degradation processes often initiate locally rather than uniformly across the coating thickness. Conventional laboratory-scale characterization techniques, such as XRD and SEM-EDS, provide reliable global information regarding phase constitution and elemental distribution; however, their spatially averaged nature limits their ability to resolve localized reactions occurring at buried interfaces. This limitation is particularly relevant for EBC systems, where CMAS-induced degradation and interfacial reactions typically originate within narrow regions that control coating lifetime. In the present study, laboratory-scale XRD successfully identified the dominant crystalline phases present in both the as-sprayed and annealed + CMAS-exposed YbDS coatings, confirming the overall phase constitution of the system. However, the technique inherently integrates diffraction information over a relatively large probed volume and is therefore insensitive to minor phases or localized transformations confined to interfacial regions. In contrast, synchrotron-based μXRD/ μXRF, performed in transmission geometry with micrometer-scale spatial resolution, enabled phase identification to be spatially assigned to individual coating layers and interfaces. This capability is particularly important for thermally sprayed EBCs, where the functional performance is governed by localized microstructural evolution rather than bulk phase composition.

For the as-sprayed YbDS coating, μXRD confirmed the presence of phase-pure YbDS within the top coat and resolved the crystallinity of the silicon bond coat and the YbDS/Si interface separately. Importantly, μXRD verified the absence of unintended interfacial reaction phases in the as-sprayed condition, demonstrating chemical stability across the interface immediately after deposition. While conventional XRD also indicated YbDS as the dominant phase, it could not isolate contributions from individual layers or exclude the presence of minor interfacial phases due to signal averaging. In addition, the spatially resolved μXRD data allowed the amorphous contribution associated with rapid solidification during plasma spraying to be assigned primarily to the YbDS top coat, which is not accessible using laboratory-scale measurements.

The annealed and CMAS-exposed coating represents a service-relevant condition, as EBC systems are routinely crystallized through high-temperature exposure either via deliberate heat-treatment or during initial engine operation. Consequently, CMAS interaction with an as-sprayed, amorphous coating does not reflect realistic operating conditions. In this study, the short CMAS exposure duration was intentionally selected to investigate the early-stage infiltration behavior of molten CMAS, which constitutes the initial and governing stage of CMAS-induced degradation. Once infiltration pathways are established, prolonged exposure leads to extensive chemical reactions and the formation of stable corrosion products, which are beyond the scope of the present work. In the annealed + CMAS-exposed coating, synchrotron μXRD and μXRF together revealed the formation of a calcium–ytterbium–silicate oxyapatite phase confined to the YbDS/Si interface. The spatial confinement of this reaction product highlights that CMAS-induced degradation initiates locally at specific microstructural features rather than uniformly throughout the coating. While laboratory-scale XRD confirmed the presence of reaction products in a global sense, it could not resolve their precise spatial distribution or distinguish whether these phases originated from the coating surface or buried interfaces. The combined μXRD/μXRF approach therefore provided critical insight into the depth and location of CMAS interaction within the multilayer EBC architecture.

Overall, the results demonstrate that synchrotron μXRD and μXRF should not be regarded as replacements for conventional laboratory techniques, but rather as complementary tools that address specific limitations associated with spatial averaging in thermally sprayed coatings. When applied to EBC systems, these techniques enable localized phase attribution, interfacial reaction mapping, and early-stage degradation analysis that are directly relevant to coating design and lifetime prediction. The present work therefore establishes the value of synchrotron microanalysis for addressing thermal spray-specific challenges associated with CMAS degradation in environmental barrier coatings.

Conclusions

In the present work, the applicability of synchrotron-based μXRD and μXRF was evaluated for SPS-based YbDS EBC coatings using an as-sprayed coating and an annealed and CMAS-exposed coating as independent case studies. Conventional laboratory-scale XRD provided reliable

global phase information but was limited in resolving layer-specific phase constitution and buried interfacial features. In contrast, μXRD enabled spatially resolved phase identification within individual coating layers and across interfaces. For the as-sprayed coating, μXRD confirmed phase-pure YbDS in the top coat, resolved the crystallinity of the silicon bond coat, and verified the absence of unintended interfacial reaction phases, demonstrating its capability even in the absence of advanced degradation. In the annealed and CMAS-exposed coating, μXRD and μXRF revealed the formation of a calcium–ytterbium–silicate oxyapatite phase confined to the YbDS/Si interface, confirming that CMAS-induced degradation initiates locally rather than uniformly across the coating. Overall, the results show that synchrotron μXRD and μXRF are effective complementary tools for resolving localized phase evolution and early-stage degradation in complex thermally sprayed environmental barrier coating systems.

Acknowledgments We would like to acknowledge our collaborators from the University of Nottingham for providing the as-sprayed and annealed+CMAS-exposed YbDS coatings, Paul Scherrer Institute for providing the synchrotron beamtime, Joakim Reuteler for preparing the FIBed samples at Scientific Center for Optical and Electron Microscopy, ETH Zurich, Switzerland. We sincerely thank Aki Piiroinen for his invaluable assistance in performing various laboratory activities. Prof. Ashish Ganvir acknowledges financial support from GREEN-BAT (Dnr 352517), co-funded by the Research Council of Finland and the European Union under the M-ERA.NET 2021 framework, as well as the SOLACE (Dnr 360540) Academy research fellowship, funded by the Research Council of Finland. He also extends his gratitude to the City of Turku for supporting his tenure-track grant. Prof. Antti Salminen acknowledges financial support through the DREAMS TEKN TOT (2600577911) project, funded by Business Finland.

Author Contributions Chinmayee Nayak was responsible for the conceptualization, data curation, formal analysis, investigation, methodology, writing–original draft, and writing–review and editing. Gidla Vinay participated in the thorough review and editing of the manuscript. Arman Hasani and Nikhil Kamboj carried out the synchrotron experiments at PSI, Switzerland, under the supervision of Malgorzata Grazyna Makowska. Arman Hasani also assisted with the analysis of the synchrotron data and writing–review and editing. Ermei Mäkilä conducted the SEM and EDS analysis on the FIBed micro-size samples at the University of Turku. The sample preparation and preliminary data were provided by Prof. Tanvir Hussain's research team, including Alex Lynam and Acacio Rincon Romero. Ebenezer Owusu actively contributed to data and provided valuable suggestions for the manuscript throughout the entire process. The idea of utilizing synchrotron techniques to investigate localized phase changes in annealed and CMAS-exposed EBC samples was initiated by Sneha Goel and Ashish Ganvir. Antti Salminen and Ashish Ganvir were responsible for manuscript review, resource coordination, and securing funding for the study.

Funding Open Access funding provided by University of Turku (including Turku University Central Hospital).

Conflict of interest The authors declare that they do not have any identifiable competing financial interests or personal relationships that might have been perceived to affect the results presented in this paper.

References

1. D.R. Clarke and C.G. Levi, Materials Design for the Next Generation Thermal Barrier Coatings, *Annu. Rev. Mater. Res.*, 2003, **33**, p 383–417. https://doi.org/10.1146/annurev.matsci.33.011403.113718
2. V.L. Wiesner, D. Scales, N.S. Johnson, B.J. Harder, A. Garg, and N.P. Bansal, Calcium–Magnesium Aluminosilicate (CMAS) Interactions with Ytterbium Silicate Environmental Barrier Coating Material at Elevated Temperatures, *Ceram. Int.*, 2020, **46**, p 16733–16742. https://doi.org/10.1016/j.ceramint.2020.03.249
3. A. Lynam, A.R. Romero, B. Zhang, S. Lokachari, F. Xu, G.J. Brewster, G. Pattinson, and T. Hussain, Abradable Ytterbium Disilicate Environmental Barrier Coatings: A Story of CMAS and Combined CMAS-Erosion Performance, *Surf. Coat. Technol.*, 2024 https://doi.org/10.1016/j.surfcoat.2024.131502
4. D. Tejero-Martin, C. Bennett, and T. Hussain, A Review on Environmental Barrier Coatings: History, Current State of the Art and Future Developments, n.d.
5. E.J. Opila, Oxidation and Volatilization of Silica Formers in Water Vapor, *J. Am. Ceram. Soc.*, 2003, **86**, p 1238–1248. https://doi.org/10.1111/j.1151-2916.2003.tb03459.x
6. A. Nieto, R. Agrawal, L. Bravo, C. Hofmeister-Mock, M. Pepi, and A. Ghoshal, Calcia–Magnesia–Alumina–Silicate (CMAS) Attack Mechanisms and Roadmap Towards Sandphobic Thermal and Environmental Barrier Coatings, *Int. Mater. Rev.*, 2021, **66**, p 451–492. https://doi.org/10.1080/09506608.2020.1824414
7. 4.4.2-2a Coatings for Superalloy Components, 1998. www.asminternational.org
8. S.R. Choi, R.C. Robinson, K.N. Lee, R.T. Bhatt, and R.A. Miller, Advanced Environmental Barrier Coatings Development for Si-Based Ceramics, 2005. http://www.sti.nasa.gov
9. G. Cao, Y.H. Wang, Z.Y. Ding, Z.G. Liu, J.H. Ouyang, Y.M. Wang, and Y.J. Wang, CMAS Hot Corrosion Behavior of Rare-Earth Silicates for Environmental Barrier Coatings Applications: A Comprehensive Review, *Heat Treat. Surf. Eng.*, 2021, **3**, p 9–28. https://doi.org/10.1080/25787616.2021.2019389
10. R. Vaßen, E. Bakan, D. Sebold, and Y.J. Sohn, Correlation of Process Conditions, Porosity Levels and Crystallinity in Atmospherically Plasma Sprayed Yb2Si2O7 Environmental Barrier Coatings, *J. Compos. Sci.*, 2021 https://doi.org/10.3390/jcs5080198
11. K. Knipe, A. Manero, S.F. Siddiqui, S. Sofronsky, P. Fouquet, S. Raghavan, C. Meid, J. Wischek, M. Bartsch, J. Okasinski, J. Almer, and A. Karlsson, Synchrotron XRD measurements of

thermal barrier coatings subjected to loads representing operational conditions of rotating gas turbine blades, in: 52nd Aerospace Sciences Meeting, American Institute of Aeronautics and Astronautics Inc., 2014: pp. 1–5. https://doi.org/10.2514/6.2014-1157.
12. F. Briki, J. Vérine, J. Doucet, P. Bénas, B. Fayard, M. Delpech, G. Grateau, and M. Ris-Kautt, Synchrotron x-ray Mcrodiffraction Reveals Intrinsic Structural Features of Amyloid Deposits in Situ, *Biophys. J.*, 2011, **101**, p 486–493. https://doi.org/10.1016/j.bpj.2011.05.055
13. P. Chakrabarti, A. Wildeis, M. Hartmann, R. Brandt, R. Döhrmann, G. Fevola, C. Ossig, M.E. Stuckelberger, J. Garrevoet, K.V. Falch, V. Galbierz, G. Falkenberg, and P. Modregger, X-ray Diffraction with Micrometre Spatial Resolution for Highly Absorbing Samples, *J. Synchrotron Radiat.*, 2022, **29**, p 1407–1413. https://doi.org/10.1107/S1600577522008025
14. E.B. Owusu, A. Rincón Romero, A. Lynam, B. Zhang, O. Gavalda-Diaz, and T. Hussain, Suspension Plasma Sprayed Ytterbium Disilicate Coatings: Phase Stability and Microstructural Evolution in Extreme Environments, *J. Eur. Ceram. Soc.*, 2024 https://doi.org/10.1016/j.jeurceramsoc.2024.116779
15. E. Bakan, D. Zhou, D.E. Mack, D. Koch, and R. Vaßen, Plasma Sprayed Duplex Ytterbium Disilicate/Monosilicate EBCs and the Transformation from Ytterbia to Ytterbium Monosilicate During Burner Rig Testing, *Corros. Sci.*, 2024 https://doi.org/10.1016/j.corsci.2024.112174
16. S. Lokachari, K. Leng, A. Rincon Romero, N. Curry, G. Brewster, A. Norton, and T. Hussain, Processing-Microstructure-Properties of Columns in Thermal Barrier Coatings: A Study of Thermo-Chemico-Mechanical Durability, *ACS Appl. Mater. Interfaces*, 2024, **16**, p 10646–10660. https://doi.org/10.1021/acsami.3c16681
17. R. Vaßen, E. Bakan, C. Gatzen, S. Kim, D.E. Mack, and O. Guillon, Environmental Barrier Coatings Made by Different Thermal Spray Technologies, *Coatings*, 2019 https://doi.org/10.3390/coatings9120784
18. E. Bakan, D. Marcano, D. Zhou, Y.J. Sohn, G. Mauer, and R. Vaßen, Yb2Si2O7 Environmental Barrier Coatings Deposited by Various Thermal Spray Techniques: A Preliminary Comparative Study, *J. Therm. Spray Technol.*, 2017, **26**, p 1011–1024. https://doi.org/10.1007/s11666-017-0574-1
19. R. Vaen, H. Kaner, G. Mauer, and D. Stöver,Suspension Plasma Spraying: Process Characteristics and Applications, *J. Therm. Spray Technol.*, 2010, **19**, p 219–225. https://doi.org/10.1007/s11666-009-9451-x
20. R. Mcpherson, A review of microstructure and properties of plasma sprayed ceramic coatings, 1989
21. A. Hasani, S. Joshi, A. Salminen, S. Goel, J. Reuteler, M.G. Makowska, and A. Ganvir, Localized Phase and Elemental Mapping in Solid-State Lithium Battery LTO Anode Thin-Film Produced by a Novel Suspension Plasma Spray Approach, *J. Therm. Spray Technol.*, 2025, **34**, p 1589–1597. https://doi.org/10.1007/s11666-025-02003-6
22. G. Ashiotis, A. Deschildre, Z. Nawaz, J.P. Wright, D. Karkoulis, F.E. Picca, and J. Kieffer, The Fast Azimuthal Integration Python Library: PyFAI, *J. Appl. Crystallogr.*, 2015, **48**, p 510–519. https://doi.org/10.1107/S1600576715004306
23. V.A. Solé, E. Papillon, M. Cotte, P. Walter, and J. Susini, A A Multiplatform Code for the Analysis of Energy-Dispersive X-ray Fluorescence Spectra, *Spectrochim. Acta B At. Spectrosc.*, 2007, **62**, p 63–68. https://doi.org/10.1016/j.sab.2006.12.002
24. D. Tejero-Martin, M. Bai, A. Rincon Romero, R.G. Wellman, and T. Hussain, Steam Degradation of Ytterbium Disilicate Environmental Barrier Coatings: Effect of Composition, Microstructure and Temperature, *J. Therm. Spray Technol.*, 2023, **32**, p 29–45. https://doi.org/10.1007/s11666-022-01473-2
25. B.T. Richards, H. Zhao, and H.N.G. Wadley, Structure, Composition, and Defect Control during Plasma Spray Deposition of Ytterbium Silicate Coatings, *J. Mater. Sci.*, 2015, **50**, p 7939–7957. https://doi.org/10.1007/s10853-015-9358-5
26. B.T. Richards, K.A. Young, F. De Francqueville, S. Sehr, M.R. Begley, and H.N.G. Wadley, Response of Ytterbium Disilicate-Silicon Environmental Barrier Coatings to Thermal Cycling in Water Vapor, *Acta Mater.*, 2016, **106**, p 1–14. https://doi.org/10.1016/j.actamat.2015.12.053
27. E. Garcia, O. Sotelo-Mazon, C.A. Poblano-Salas, G. Trapaga, and S. Sampath, Characterization of Yb2Si2O7–Yb2SiO5 Composite Environmental Barrier Coatings Resultant from in Situ Plasma Spray Processing, *Ceram. Int.*, 2020, **46**, p 21328–21335. https://doi.org/10.1016/j.ceramint.2020.05.228
28. D. Tejero-Martin, A.R. Romero, R.G. Wellman, and T. Hussain, Interaction of CMAS on Thermal Sprayed Ytterbium Disilicate Environmental Barrier Coatings: A Story of Porosity, *Ceram. Int.*, 2022, **48**, p 8286–8296. https://doi.org/10.1016/j.ceramint.2021.12.033
29. J.L. Stokes, M.J. Presby, R.I. Webster, J. Setlock, and B.J. Harder, Thermochemical/thermomechanical synergies in high-temperature solid particle erosion of cmas-exposed ebcs, n.d
30. J.L. Stokes, B.J. Harder, V.L. Wiesner, and D.E. Wolfe, Mechanisms of Apatite Formation in Reactions of Yb 2-2x Gd 2x Si 2 O 7 With CMAS, 2024. http://www.sti.nasa.gov